Hydrous SiO$_2$ in subducted oceanic crust and H$_2$O transport to the core-mantle boundary

Yanhao Lin [a,b,c,*], Qingyang Hu [a,**], Michael J. Walter [b,**], Jing Yang [b], Yue Meng [d], Xiaolei Feng [a,e], Yukai Zhuang [a], R.E. Cohen [b], Ho-Kwang Mao [a,**]

HPSTAR
1513-2022

[a] *Center for High Pressure Science and Technology Advanced Research, Beijing, 100193, People's Republic of China*
[b] *Earth and Planets Laboratory, Carnegie Institution for Science, Washington, DC 20015, United States of America*
[c] *Department of Earth Sciences, Faculty of Science, Vrije Universiteit Amsterdam, De Boelelaan 1085, 1081 HV Amsterdam, The Netherlands*
[d] *HPCAT, X-ray Science Division, Argonne National Lab, Lemont, IL 60439, United States of America*
[e] *Department of Earth Sciences, University of Cambridge, Downing Street, Cambridge, CB2 3EQ, UK*

ARTICLE INFO

ABSTRACT

Subduction of oceanic lithosphere transports surface H$_2$O into the mantle. Recent studies show that dense SiO$_2$ in the form of stishovite, an abundant mineral in subducted oceanic crust at depths greater than $\sim$270 km, has the potential to host and transport a considerable amount of H$_2$O into the lower mantle, but the H$_2$O storage capacity of SiO$_2$ phases at high pressure and temperature remains uncertain. We investigate the hydration of stishovite and its higher-pressure polymorphs, β-stishovite and seifertite, with *in situ* X-ray diffraction experiments at high pressures and temperatures. The H$_2$O contents in SiO$_2$ phases are quantified based on observed increases in unit cell volume relative to the anhydrous SiO$_2$ system. Density functional theory (DFT) computations permit calibration of water content as a function of volume change based on interstitial substitution of H$_2$O. Regression of our experimental data indicates an H$_2$O storage capacity in stishovite of $\sim$3.5 wt% in the transition zone and shallow lower mantle, decreasing to about 0.8 wt% at the base of the mantle. We find that SiO$_2$-bearing subducted oceanic crust can accommodate all the H$_2$O in slab lithosphere that survives sub-arc dehydration. Hydration of silica phases in subducted oceanic crust and their unparalleled capacity to host significant amounts of H$_2$O even at high mantle temperatures provides a unique mechanism for transport and storage of water in the deepest mantle.

1. Introduction

Subduction of oceanic lithosphere drives material circulation in Earth's interior and provides an important host for transporting H$_2$O into mantle. When added to mantle rocks H$_2$O significantly affects chemical and physical properties, including mineral phase relations (Iwamori, 2004), melting temperatures (Hirschmann, 2006) and electrical conductivity (Yoshino et al., 2008) and is implicated as a potential trigger of intermediate and deep-focus earthquakes (Omori et al., 2004). Silica (SiO$_2$) crystallizes as a major component in subducted oceanic crust and sediment ($\sim$10–30 wt%) (Irifune et al., 1994; Ono, 1998; Perrillat et al., 2006) and undergoes several polymorphic phase changes as the slab subducts

to the core-mantle boundary (CMB). In the anhydrous system, stishovite, a dense tetragonal SiO$_2$ polymorph, is stable in oceanic crust from about 250 to 1500 km, where it converts to an orthorhombic CaCl$_2$-structured phase, hereafter referred to as β-stishovite, through a second-order displacive phase transition (Fischer et al., 2018; Kingma et al., 1995). The β-stishovite phase subsequently converts to seifertite with an α-PbO$_2$-structure near the base of the lower mantle (Sun et al., 2019).

Recent high-pressure experiments have shown that stishovite and β-stishovite may host wt% levels of H$_2$O in their crystal structures (Lin et al., 2020; Nisr et al., 2020, 2017b; Spektor et al., 2016, 2011). Results from hydrothermal synthesis of stishovite in the multi-anvil apparatus (e.g., $\sim$10 GPa, 350–550 °C) indicate several wt% H$_2$O in stishovite based on thermogravimetric analysis of recovered samples (Nisr et al., 2017b; Spektor et al., 2016, 2011). H$_2$O contents in stishovite produced in recent laser-heated DAC experiments have been estimated from observations of expanded unit cell volumes relative to anhydrous stishovite using a calibration based on measurements made at 1 atm (Lin et al., 2020; Nisr

* Corresponding author at: Center for High Pressure Science and Technology Advanced Research, Beijing, 100193, People's Republic of China.
** Corresponding authors.
E-mail address: yanhao.lin@hpstar.ac.cn (Y. Lin).

et al., 2020, 2017b). Based on unit cell volumes measured at high pressure in the experiments by Lin et al. (2020) this calibration predicts >10 wt% H_2O in some cases, values that seem excessively high and call into question the validity of the calibration at high pressures.

These results are in stark contrast to those from earlier studies on stishovite hydration that found much lower H_2O contents. Pawley et al. (1993) measured <10 ppm H_2O in pure SiO_2 and about 80 ppm H_2O in Al-bearing stishovite synthesized at 10 GPa, 1200 °C and suggested hydrogen incorporation coupled to Al^{3+} substitution giving rise to oxygen defects, e.g. $2Si = 2Al + O_v$. Bolfan-Casanova et al. (2000) found very similar results between alumina-free and alumina-bearing stishovite equilibrated with hydrous melts (2–72 ppm H_2O) at 15 to 21 GPa, 1500 °C, with H_2O content correlated with alumina content. Chung and Kagi (2002) synthesized stishovite from hydrous glass at 10–15 GPa (1200–1400 °C) and found a correlation between H_2O content and trivalent cations and measured a maximum of 844 ppm H_2O. Bromiley et al. (2006) synthesized stishovite at 15 GPa, 1500 °C under H_2O-saturated conditions and reported 3–456 ppm H_2O in alumina free and alumina-bearing stishovite and discussed H incorporation in stishovite as a function of alumina content. Litasov et al. (2007) measured the H_2O contents of stishovite synthesized at 20–25 GPa and 1200–1800 °C and found that hydrogen can occupy 40% of vacancies created by incorporation of Al^{3+} at 20 GPa, reporting values of <30 ppm in Al-free stishovite and up to ~3000 ppm in stishovite with 4.4 wt% Al_2O_3. All of these studies were performed in multi-anvil apparatus under nominally H_2O saturated conditions, with sample water contents measured by FTIR on P-T quenched samples. In contrast, Panero et al. (2003) used the laser-heated diamond anvil cell to synthesize stishovite in a basalt composition with 0.2 wt% H_2O in the bulk at pressures of 28–60 GPa and up to 4000 °C and measured maximum water contents of 500 ppm using synchrotron FTIR on P-T quenched samples.

It is challenging to understand how different studies can produce such widely disparate results, with differences of the order several orders of magnitude for the H_2O capacity of stishovite. One commonality among previous studies finding low H_2O in stishovite is that H_2O contents were measured on P-T quenched samples at ambient conditions (e.g., 1 atm, ~300 K). For example, Lin et al. (2020) showed that upon decompression from high pressure, the difference in unit cell volume observed at high pressure diminishes below about 10 GPa, approaching the anhydrous volume (see Supplementary Material for further discussion). Fig. 1 shows measured unit cell volumes at 1 atm, 300 K, for pressure-temperature quenched hydrous stishovite synthesized in the experiments of Spektor et al. (2011, 2016) and Nisr et al. (2017b) in the multi-anvil apparatus compared to measurements of anhydrous stishovite. The hydrous stishovite data show a wide range in unit cell volume for samples synthesized at nominally similar conditions, sometimes overlapping cell volumes of anhydrous stishovite, other times showing large volume excesses. Also shown on Fig. 1 is the even larger range in unit cell volumes found in the DAC experiments of Nisr et al. (2020) measured on samples decompressed to ambient conditions.

Considering all these disparate observations, currently the extent of H_2O solubility in dense SiO_2 polymorphs at high pressure and temperature and the mechanism of H_2O incorporation remains highly uncertain. To further investigate H_2O incorporation in high-pressure SiO_2 polymorphs we combine *in-situ* laser heating and high-pressure X-ray diffraction measurements with first-principles theoretical calculations to constrain the phase relations and H_2O storage capacity (e.g., H_2O content at saturation) of stishovite, β-stishovite and seifertite at 44–152 GPa and ~1380–3300 K.
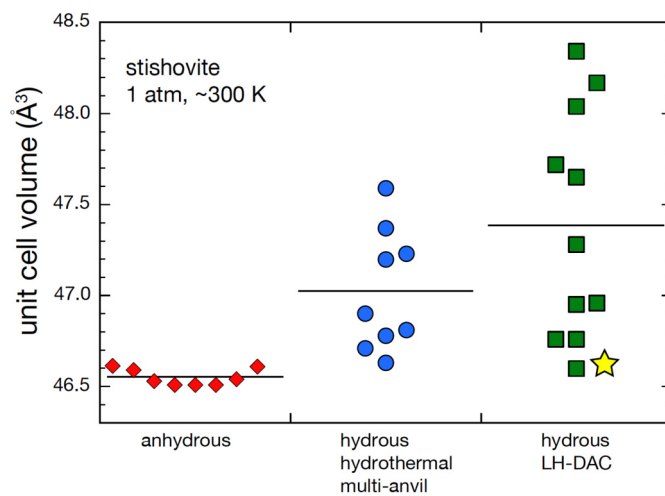

Fig. 1. Unit cell volumes measured at ambient conditions (1 atm, ~300 K) for anhydrous stishovite (red diamonds) and hydrous stishovite produced hydrothermally at ~10 GPa, 350–550 °C (blue circles, Spektor et al., 2011, 2016; Nisr et al., 2017b) in the multi-anvil apparatus and at higher pressures and temperatures (~24–67 GPa; ~1450–2100 K) in the diamond anvil cell (yellow star, Lin et al., 2020 extrapolated; green squares, Nisr et al., 2020). Horizontal lines show group averages. Uncertainties in individual measurements typically ~0.2 $Å^3$.

2. Materials and methods

2.1. Starting materials and experimental design

Starting materials with H_2O contents of 0.5 wt% (experiment S_241), 1.2 wt% (S_242) and 3.5 wt% (C_188) were synthesized as mixtures of amorphous SiO_2 (1 μm grain size, purity 99.999%) and silic acid ($SiO_2 \cdot 0.6H_2O$, 15.2 wt% H_2O) in calculated proportions and ground in an agate mortar for 4–6 hours. The starting material with 15.2 wt% H_2O was only silicic acid (experiments C_283 and C_154R). About 10 wt% amorphous Pt or Au powder was added to the mixture for infrared laser absorption and pressure calibration in laser heating experiments.

Samples were loaded into symmetric diamond anvil cells. In experiments S_241, S_242 and C_188 samples were loaded in a 120 μm diameter hole in a rhenium gasket indented by diamond anvils with 250 μm diameter culets. In experiment C_283, the sample was loaded in a 100 μm diameter hole in a rhenium gasket indented by diamond anvils with 200 μm diameter culets. In experiment C_154R, the sample was loaded in a 45 μm diameter hole in a rhenium gasket indented by diamond anvils with 90 μm diameter culets beveled from 400 μm culets. Except for sample C_283 with Au powder, the other four samples were mixed with Pt black. Pressures were determined before and after heating by the self-consistent equations of state (EOS) of Pt or Au (Fei et al., 2007), and the uncertainty in calibrated pressure is estimated to be of the order 1 to 2 GPa.

2.2. High pressure-temperature experiments and in situ X-ray diffraction

Diamond anvil cell samples were laser-heated and examined *in situ* at high pressures and temperatures by synchrotron x-ray powder diffraction at the High Pressure Collaborative Access Team (HPCAT) beamline (16-ID-B) of the Advanced Photon Source, Argonne National Laboratory and at the BL15U1 beamline, Shanghai Synchrotron Radiation Facility (SSRF) in China. The diameter of the laser heating spot was typically 20 to ~30 μm in the flat top area created with a focused yttrium lithium fluoride laser using a double-sided geometry that minimizes both radial and axial temperature gradients. Samples were heated at each temperature

typically for 10 to 15 minutes. Temperatures were determined by fitting the thermal radiation from the central portion of the heated spot to the Planck radiation function (Meng et al., 2006; Hirao et al., 2020) with precision of individual measurements of <10 K and overall uncertainty of quoted temperatures considering accuracy and temperature fluctuations during heating of ∼50–100 K.

X-ray diffraction (XRD) patterns were acquired at each pressure both at high temperature and after quenching to ambient temperature (see Supplementary Material Fig. 1 for example diffraction patterns). Monochromatic X-rays with a wavelength of 0.4066 Å at HPCAT (2.9×5.4 μm² beam size) and 0.6199 Å at SSRF (1.0×3.0 μm² beam size) were aligned with the laser heated spot for powder diffraction measurements. Sample to detector distance was calibrated using a CeO with calibrant and samples aligned to the center of rotation. At HPCAT, the diffraction patterns are recorded with a Pilatus 1M detector with typical exposure time of 10–15 seconds. At SSRF, the diffraction patterns were collected with a MAR345 CCD detector with exposure time of 60 seconds. All the diffraction data were reduced to 2-theta versus intensity using the Dioptas software (Prescher and Prakapenka, 2015).

2.3. Density functional theory (DFT) calculations

Incorporation of water in stishovite and β-stishovite was simulated using density functional theory with CASTEP and CP2K codes. Relaxations were performed as function of pressure at zero temperature (static) and first-principles molecular dynamics (FPMD) at high temperature. We used supercells containing different hydrogen contents and in various configurations.

Calculations for hydration of stishovite at 50 GPa and zero kelvin were performed using CASTEP (Clark et al., 2005) and a PBE-GGA exchange-correlation potential with an on-the-fly pseudo potential with a cut-off energy of 520 eV. Different supercell sizes were used to fit the related water contents (see Table S2). The water molecule was placed within the channels that run parallel to the crystallographic z-axis in the stishovite unit cell and, to test the range of possible substitutions, the molecule was located at three different initial positions each with three different initial orientations before the simulation cell was relaxed, with the constraint that the space group was maintained in each case to represent a mean field tetragonal structure. We found that the lowest energy configurations were those in which the molecule was centered within the octahedral interstitial site, with only very small differences in energies (∼3 meV/atom) of the relaxed cells for orientations of O-H bonds parallel to x-, y- and z-axes. The average unit cell volume defined by the three different orientations was used as a representative of that of hydrous stishovite with (potentially) orientationally disordered interstitial water molecule centered on the channel interstitial site. Four different water contents were simulated, corresponding to supercells of 3×3×3 (0.55 wt.% H_2O), 2×2×3 (1.23 wt.% H_2O), 1×3×3 (1.64 wt.% H_2O) and 1×2×3 (2.43 wt.% H_2O) each containing one interstitial water molecule. We also simulated incorporating hydrogen in stishovite by substituting $4H^+$ for Si^{4+} ('hydrogarnet' substitution), and in contrast to the interstitial substitution, found that the unit cell volume decreases by 0.17% relative to dry stishovite.

High temperature and pressure unit cell volumes for hydration of stishovite and β-stishovite were performed using NPT first-principles molecular dynamics with flexible cells (constant stress) within DFT using the CP2K code. Simulations were at least 10,000 time steps with time increments of 0.5 or 1 fs. The DF2 non-local wan der Waals exchange-correlation functional was used. Simulations were performed at 35, 70, 100 and 135 GPa at ∼300 K to 2200 K. We simulated interstitial substitution with one H_2O in a cell with 165 atoms ($54SiO_2$:H_2O), inter-crystalline substitution ($2H^+ + O^{2-} \rightarrow 2O^{2-} + Si^{4+}$) with $2H^+$ in a cell with 162 atoms

($53SiO_2$:H_2O), and the 'hydrogarnet' substitution ($4H^+ \rightarrow Si^{4+}$) in a cell with 165 atoms ($53SiO_2$:$2H_2O$). Anhydrous SiO_2 was simulated using a cell with 162 atoms (54 SiO_2). Results are provided in Supplementary Table 1.

3. Results

Unit cell parameters of SiO_2 phases are summarized in Supplementary Table 2. We compared measured cell volumes in the system SiO_2-H_2O to the calculated cell volumes of anhydrous silica phases at each pressure and temperature using appropriate thermal equations of state (EoS) (Andrault et al., 2003; Fischer et al., 2018; Grocholski et al., 2013; Sun et al., 2019) to calculate the percent relative change in unit cell volume:

$$\Delta V / V_{dry}\% = (V_{hydrous} - V_{dry})/V_{dry} \times 100 \tag{1}$$

Consistent with previous studies in the SiO_2-H_2O system, diffraction patterns obtained at high pressure and temperature or at high pressure but quenched to ambient temperature (∼300 K) reveal significant volume expansion for stishovite (up to ∼6.9%) and β-stishovite (up to ∼5.1%) (Lin et al., 2020; Nisr et al., 2020, 2017a), and we observe lesser but still positive volume expansion in seifertite (∼1.1–1.7%). These large relative volume expansions are attributed to the incorporation of H_2O in some form in the structures of the SiO_2 phases.

3.1. The H_2O storage capacity of stishovite: experimental constraints

We establish the magnitude of the H_2O storage capacity through a series of experiments with varying H_2O contents in the starting compositions at near constant pressure and temperature (∼50 ±6 GPa and ∼1800 ±70 K) where stishovite is observed to be the stable polymorph. In principle, incorporation of H_2O will cause a systematic change in unit cell volume at constant pressure and temperature but once a phase reaches H_2O saturation its unit cell volume will remain constant even as the bulk system H_2O content increases. As shown on Fig. 2, we observe a linear relationship between the volume change of stishovite up to ∼3.5 wt% H_2O in the starting material. In our starting composition with the highest water content of 15.2 wt% H_2O, chosen to be very high to assure H_2O saturation, we find effectively the same maximum relative volume change of ∼6.5% as in experiments with 3.5% H_2O, indicating stishovite is saturated at ∼3.5% wt% H_2O at ∼50 GPa and 1800 K.

3.2. H_2O incorporation mechanisms in high pressure SiO_2 phases: ab initio calculations

The H_2O incorporation mechanism is unknown from diffraction measurements and there are many potential substitution mechanisms that may operate simultaneously. We test three candidates for producing the observed unit cell volume systematics observed in Fig. 1: (1) the "hydrogarnet" substitution where four hydrogen atoms substitute for a silicon atom, $4H^+ \rightarrow Si^{4+}$, which has been suggested as a stishovite hydration mechanism (Nisr et al., 2020, 2017b; Spektor et al., 2011); (2) incorporation of H_2O through inter-crystalline substitution ($2H^+ + O^{2-} \rightarrow 2O^{2-} + Si^{4+}$); (3) incorporation of interstitial H_2O in the stishovite lattice ($SiO_2 \cdot xH_2O$). We use density functional theory (DFT) combined with molecular dynamics calculations to determine the effect of these substitutions on unit cell volume at pressures and temperatures ranging from 35 to 135 GPa and 0 to ∼2200 K (Supplementary Table 1).

Fig. 2b compares the volume changes predicted in DFT calculations with the experimental results. The hydrogarnet substitution
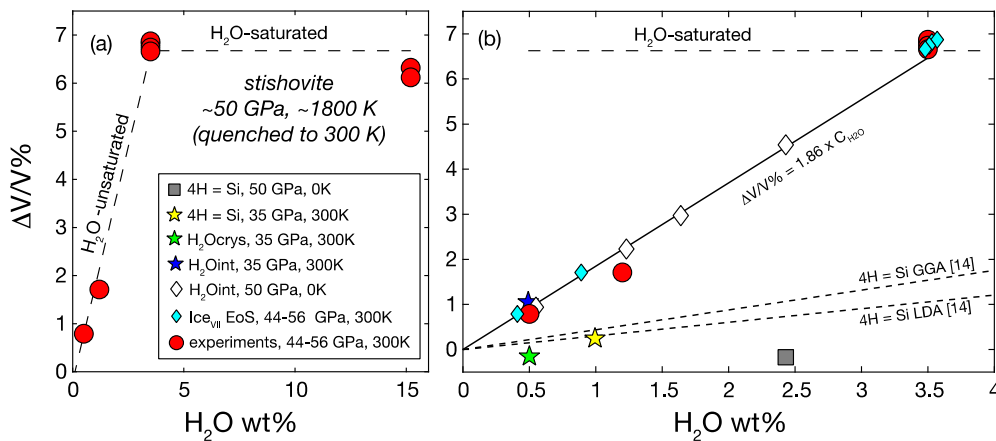
Fig. 2. (a) The change in unit cell volume of hydrous stishovite relative to anhydrous stishovite at the same pressure and temperature ($\Delta V/V\%$) versus H_2O content in the bulk starting compositions. Red symbols are experiments at 50±6 GPa, 1800±70 K (Supplementary Table 2). The constant volume change above ∼3.5 wt% H_2O indicates H_2O saturation. (b) The relative volume change of stishovite versus H_2O content comparing experimental results with predictions from DFT and DFT-MD calculations and ice VII equation of state calculations, this study. Also shown are the 0 K DFT calculations for the hydrogarnet substitution (4H = Si) from Nisr et al. (Nisr et al., 2020), which are in general agreement with our calculations. Note how the interstitial substitution produces a volume change that reproduces the experimental trend but the hydrogarnet substitution cannot, producing a much smaller volume expansion. Also shown (cyan diamonds) is the expected volume expansion in stishovite by adding together the volume of anhydrous stishovite at ∼50 GPa and 300 K with the ice VII volume at the same pressure and temperature using its EoS (Wolanin et al., 1997). If H_2O is incorporated into stishovite as interstitial H_2O its stable phase is ice VII at 300 K and to first order their additive volumes may approximate the effect volume change in stishovite. Remarkably, we observe a nearly one-to-one correlation between the predicted H_2O content using the ice VII EoS and those for interstitial substitution based on our ab initio calculations.

produces a small volume change, in good agreement with previous calculations (Nisr et al., 2020), but much less than observed in our experiments. Similarly, inter-crystalline substitution of H_2O produces a small negative volume change at 300 K. In contrast, the large change in volume predicted for interstitial substitution of H_2O at 50 GPa, 0 K, closely approximates the trend of our experimental data. On this basis we use our DFT molecular dynamics results for interstitial H_2O substitution to calibrate the minimum H_2O contents in stishovite and β-stishovite in our experiments. Caracas and Panero (2017) suggested that hydrogen diffusion in ringwoodite may occur through a hydrogarnet substitution mechanism. In our FPMD simulations at 2000 K and 35 GPa, we find no diffusion of H in interstitial H_2O over our 10 ps simulations, nor do we find such in the hydrogarnet substitutions. In addition, we do not anticipate that quantum effects will play a large role in hydrous stishovite.

To further test the veracity of the interstitial substitution model and calibration, we estimated the expected volume expansion in stishovite by adding together the volume of anhydrous stishovite at ∼50 GPa and 300 K with the ice VII volume at the same pressure and temperature using its EoS (Wolanin et al., 1997). If H_2O is incorporated into stishovite as an interstitial H_2O molecule its stable phase is ice VII at 300 K, and to first order their additive volumes may approximate the effect of interstitial incorporation of H_2O. The results are plotted on Fig. 2b (cyan diamonds) and, remarkably, we observe a nearly one-to-one correlation between the predicted H_2O content using the ice VII EoS and those for interstitial substitution based on our ab initio calculations. This consistency further supports that the large volume excesses we observe result primarily through interstitial incorporation of molecular H_2O at high pressure.

3.3. An H_2O in stishovite and β-stishovite calibration based on interstitial substitution

We regressed the H_2O content in the sixteen DFT data points to a simple linear function of relative volume change ($\Delta V/V_{dry}\%$), pressure and temperature. We find no statistically relevant pressure or temperature effects (see Supplementary Table 3), and the concentration of H_2O (C_{H2O}) is well-fitted over the entire *P-T* range only as a function of the relative volume change:

$$C_{H_2O}\,(\text{wt}\%) = 0.5334 \times (\Delta V/V_{dry}\%) + 0.0124\,(\text{R}^2 = 0.99) \qquad (2)$$

Because other substitution mechanisms have only a relatively minor effect on unit cell volume, the H_2O contents calculated based on interstitial substitution alone is a minimum because other substitution mechanisms may still operate but be hidden with respect to volume change.

Our ab initio calculations show that the volume change for interstitial H_2O substitution mimics closely the observed volume changes in our experiments at high pressure and temperature with known bulk water contents (Fig. 2b). Therefore, based on our DFT calibration we predict the water content in stishovite and β-stishovite in our experiments from their relative volume changes using equation (2), with results tabulated in Supplementary Table 2. Equation (2) is not valid for seifertite, and although we observe a generally smaller but positive relative volume change for seifertite indicating some H_2O storage capacity, likely in the range of 1 wt% or less, we currently cannot accurately assess its H_2O content.

In the study of Lin et al. (2020) the water content of hydrous stishovite was estimated using the 1 atmosphere, 300 K calibration of Nisr et al. (2017b). The calibration of Nisr et al. was developed on the basis of hydrous stishovite synthesized in experiments by Spektor et al. (2016) in the multi-anvil apparatus under hydrothermal conditions (∼10 GPa, 350–550 °C). Nisr et al. fit a linear relation to the observed volume change ($V_{hydrous}$-V_{dry}) and the water contents of stishovite. Based on our new results we find that applying the Nisr et al. calibration for our experiments and using volume data at high pressures and temperatures is not appropriate. For example, application of the Nisr et al. calibration to our hydrous stishovite synthesized in this study at 53 GPa (C_188) yields ∼13 wt% water, which is more than three times the water content in the starting material. Supplementary Table 4 gives the water content of hydrous stishovite in experiments reported by Lin et al. (2020) using the ab initio calibration developed in this study compared to values calculated using the Nisr et al. (2017b) calibration. We find that the water contents are systematically overestimated by nearly a factor of four in the study of Lin et al. (2020).

3.4. The effects of H_2O on phase relations

Having established that the starting mixture with 15.2 wt.% H_2O has far more H_2O than required to saturate SiO_2, we now
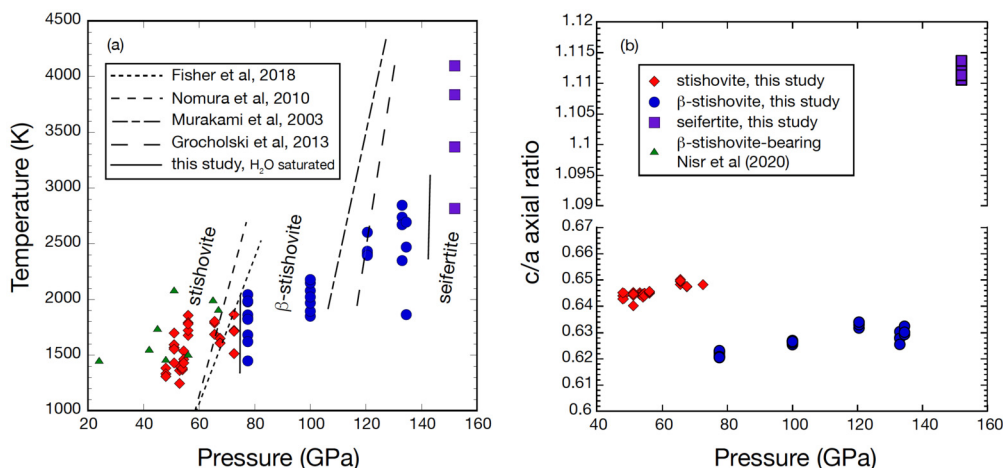
Fig. 3. (a) Pressure-temperature plot showing experiments in this study relative to experimentally determined phase boundaries in the anhydrous SiO_2 system (Fischer et al., 2018; Grocholski et al., 2013; Murakami et al., 2003; Nomura et al., 2010). We observe little difference in the stishovite to β-stishovite transition between the hydrous and anhydrous systems, whereas the β-stishovite to seifertite phase boundary is found to be ~20 GPa higher in pressure in the hydrous system. Also shown are experiments from Nisr et al. (2020) in which β-stishovite is reported to co-occur with stishovite at high pressure and temperature. (b) Pressure vs c/a ratios of stishovite, β-stishovite and seifertite in our experiments based on measurements taken at high pressure and temperature. The phase transitions are well distinguished by abrupt changes in the c/a axial ratios of the SiO_2 polymorphs.

present results for the effect of pressure and temperature on the phase relations at H_2O-saturated conditions. As shown on Fig. 3, the phase transition boundaries at high temperature under H_2O-saturated conditions were bracketed between stishovite and β-stishovite at ~75 GPa and between β-stishovite and seifertite at ~145 GPa.

The stishovite to β-stishovite transition results in a small but abrupt decrease in c/a axial ratio as tetragonal stishovite distorts to orthorhombic β-stishovite, whereas the transition to the seifertite structure results in a large increase (Fig. 3b). The transition boundary between stishovite and β-stishovite in our experiments is not significantly shifted from the dry silica system (e.g., ~74 GPa and ~1900 K) (Fischer et al., 2018), consistent with our observation that stishovite and β-stishovite have approximately the same H_2O content at the transition. We estimate the transition to seifertite at a pressure of ~145 GPa, about 20 GPa higher than in the dry system (Sun et al., 2019), suggesting a larger H_2O capacity in β-stishovite than in seifertite, although we do not have a tight constraint on the phase boundary.

In contrast to our results, Nisr et al. (2020) observe that the stishovite to β-stishovite transition occurs at much lower pressure in the SiO_2-H_2O system and that there is a large pressure range over which these two phases coexist (e.g., the phase transition becomes first order rather than second-order as in the anhydrous system). Experiments reported by Nisr et al. (2020) contain either a mixture of stishovite and β-stishovite or just β-stishovite. As shown on the example diffraction patterns in Figure S1 and exhibited by the abrupt changes in axial ratios in Fig. 3, in our study we do not find compelling evidence for co-existence of stishovite and β-stishovite. We do not have a good explanation for these different observations and more work is needed to determine the effect of H_2O on the phase transition. However, we note that what is apparent and consistent in both studies is that stishovite and β-stishovite each contain wt% levels of H_2O at saturation, and our results indicate that across the transition there is no statistically significant change in H_2O storage capacity. We also did not detect SiO_2 in the NiAs-type structure at pressures above ~60 GPa as in Nisr et al. (2020).

3.5. The effects of pressure and temperature on H_2O storage capacity

On the basis of calibrated H_2O contents in experiments with 15.2 wt% H_2O in the starting composition (e.g., saturated), we
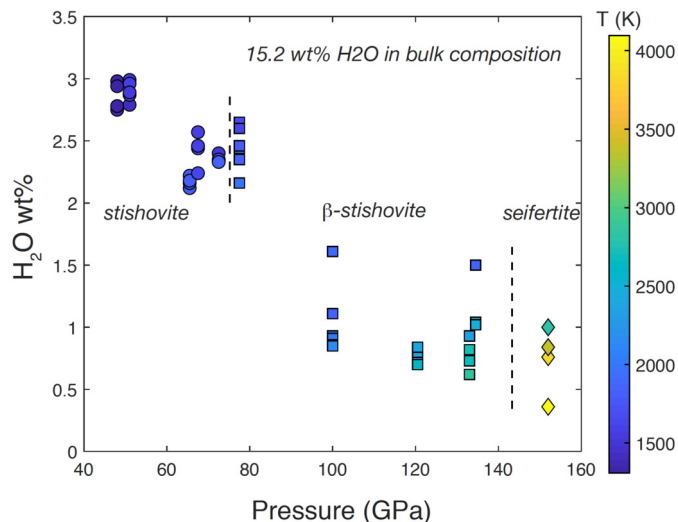

Fig. 4. H_2O content in experimental SiO_2 phases produced in the bulk composition with 15.2 wt% H_2O based on our DFT calibration. The symbols are colored for temperature according to the scale bar. Data are provided in Supplementary Table 2.

can now assess if there is a discernable effect of pressure and/or temperature on H_2O storage capacity. In run C_283 experiments were made at pressures of 48–102 GPa and temperatures of ~1300–2200 K, and in run C_154R at 97–152 GPa and ~1850–4100 K. The observed relative volume changes obtained from high-pressure and high-temperature diffraction and the corresponding H_2O contents are provided in Supplementary Table 2. H_2O contents as a function of pressure and temperature are shown in Fig. 4. The data indicate generally smaller volume changes and lower H_2O contents in the higher-pressure experiments, and while these experiments are generally at higher temperatures, experiments at ~2000 K were made over a wide range of pressure.

We evaluated whether there is a statistically discernable pressure or temperature effect on the H_2O storage capacity in stishovite and β-stishovite by regressing the ab initio calibrated H_2O contents in the high pressure-temperature experiments with 15.2 wt% H_2O to a general linear equation and a second order polynomial as a function of pressure and temperature. We fit all the data together and by fitting the data for stishovite independently of data

for β-stishovite, while inspecting the importance of variables using stepwise regression (see Supplementary Table 3). We find that fitting all the data simultaneously to a regression that is linear in pressure and temperature provides the best overall fit statistics (adjusted $R^2 = 0.83$; see Supplementary Fig. 3) resulting in the equation:

$$C_{H_2O} \, (\text{wt\%}) = -0.0191 \times P \, (\text{GPa}) - 0.00057 \times T \, (\text{K}) \\ + 4.6527 \, (R^2 = 0.83) \tag{3}$$

The regression predicts a dominant pressure dependence and a weak temperature dependence, and we use this expression to estimate the water content in subducted lithosphere in our discussion of water transport into the deep mantle.

4. Discussion

4.1. Water transport to the deep mantle in silica phases

A silica phase is expected to be absent from the mineral assemblage in Earth's average mantle because the Mg/Si ratio of primitive upper mantle peridotite is greater than unity ($\sim$1.1) (McDonough and Sun, 1995). In contrast, oceanic crustal rocks (e.g., basalt, gabbro, terrigenous pelagic sediment) have Mg/Si less than unity (Gale et al., 2013) and, therefore, silica phases can stabilize at high pressure in the crustal portion of subducted lithosphere (hereafter subducted crust refers to metabasalt + metasediment). Unique among hydrated crustal minerals, silica phases are stable at mantle pressures and temperatures all the way to the core-mantle boundary (CMB) and so represent potentially important hosts for carrying and storing H_2O to the deep interior. Here we assess the capacity and possible mechanisms for silica phases to transport water into the deep mantle in the crust of subducted lithosphere.

H_2O is added to oceanic crust and sediment through hydration near the slab surface and hydrothermal alteration of basalt at mid-ocean ridges (Alt et al., 2013; Alt and Teagle, 2003). Plate-bending at the outer rise results in fracture development in the deforming plate, with fractures penetrating through the crust and extending some 20–30 km into the slab mantle allowing seawater to circulate deeply to hydrate deeper crust and mantle lithosphere (Faccenda, 2014; Wada et al., 2012). Estimates for H_2O bound in hydrous phases and subducted into the mantle based on modern day subduction rates are of the order 0.7 to 1.8×10^{12} kg/yr (Hacker, 2008; Rupke et al., 2004; Schmidt and Poli, 2003; van Keken et al., 2011).

How much subducted H_2O is released into the shallow upper mantle wedge beneath island arc volcanos depends on the phase equilibria of the hydrated rock composition (e.g., metabasalt, metaperidotite, metasediment) and the thermal structure of the subducting slab. Models of slab dehydration in modern subduction zones that consider these factors indicate that dehydration of hydrous phases in oceanic crust and mantle is relatively efficient beneath the volcanic front with, on average, more than half of the bound water released from slabs into the mantle at depths <150 km (Hacker, 2008; Rupke et al., 2004; Schmidt and Poli, 2003; van Keken et al., 2011). For example, in the study by van Keken et al. (2011), about two-thirds of the subducted H_2O is removed from subducted slabs by a depth of $\sim$230 km, with an estimated 2.2 to 3.4×10^{11} kg/yr subducted beyond this depth split in an $\sim$2:1 ratio between the crust and mantle portions of the slab. We use these estimates to assess the role of SiO_2 phases in transporting H_2O in subducting lithosphere as it transits beyond 230 km and through the transition zone and into the lower mantle, recognizing that absolute H_2O fluxes are model dependent and based on modern subduction rates.

In the crustal portion of the slab phase relations for hydrous MORB and sediment show that phengite and lawsonite are the primary hosts for H_2O at depths beyond 150 km in cooler slabs, but dehydration of these phases is complete by about 300 km (Okamoto and Maruyama, 2004; Poli and Schmidt, 2002). This deeper dehydration would remove most of the remaining H_2O from oceanic crust to be released in the upper mantle, estimated at $\sim$2 $\times 10^{11}$ kg/yr. In the sediment portion of the crust topaz-OH and phase egg constitute a minor portion of the mineral assemblage beyond 300 km and may host $\sim$0.5 wt% H_2O (Ono, 1998). In the basaltic portion of the crust no hydrous phases were detected beyond lawsonite breakdown by Okamoto and Maruyama (2004) or Ono (1998). However, recent work indicates that an Fe-Ti oxyhydroxide solid solution may crystallize under water-saturated conditions in metabasalt at transition zone conditions (Liu et al., 2018; Nishihara and Matsukage, 2016). However, we note that at 13 GPa this phase was absent in hydrous metabasalt in the experiments of Liu et al. (2018) but was present at 24 GPa. Oceanic crust has only a relatively minor capacity to transport H_2O beyond 300 km in nominally anhydrous phases like garnet and clinopyroxene (e.g., <0.1 wt% or $\sim$5 $\times 10^{10}$ kg/yr).

Hydrous stishovite in subducted oceanic crust provides a mechanism for retaining significant H_2O at 300 km and throughout the deep upper mantle and transition zone and into the lower mantle. A free silica phase begins to crystallize in basaltic oceanic crust as coesite at $\sim$150 km, transforming to stishovite at $\sim$250 km. Experiments indicate that in a mid-ocean ridge basalt (MORB) composition stishovite constitutes $\sim$10 wt% of the mineral assemblage by 9 GPa ($\sim$270 km), increasing to as much as 20 wt% or more in the transition zone and lower mantle (Okamoto and Maruyama, 1999; Ono, 1998; Ono et al., 2001; Perrillat et al., 2006). In siliceous oceanic sediments a silica phase constitutes $\sim$30% of the mineral assemblage throughout the upper mantle and into the lower mantle (Irifune et al., 1994; Ono, 1998).

In the mantle portion of cooler slabs, H_2O can be transported to depths beyond 300 km in post-serpentine phases (Phase A, Phase E and Phase D; $\sim$1 $\times 10^{11}$ kg/yr) in modern subduction zones (Iwamori, 2004; Komabayashi and Omori, 2006; Rupke et al., 2004; Shirey et al., 2021; van Keken et al., 2011). However, subsequent dehydration of hydrated mantle occurs either in the transition zone as slabs stagnate (Bina, 1997), or in the shallow lower mantle when hydrous phases like ringwoodite, Al-poor Phase D and superhydrous Phase B dehydrate (Ohtani, 2015). Thus, deep dehydration of subducting mantle lithosphere in the shallow lower mantle potentially releases most of its H_2O cargo, with the residual H_2O content dependent on the storage capacity of nominally anhydrous phases (e.g., $\sim$1000 ppm H_2O or less).

Fig. 5 shows the predicted H_2O storage capacity in stishovite and β-stishovite and in bulk subducted oceanic crust along mantle and average modern slab crust geotherms (Katsura et al., 2010; Shirey et al., 2021; Walter, 2021). At 10 GPa, we estimate that stishovite has an H_2O storage capacity of $\sim$3.7 wt%, progressively reducing to $\sim$0.7 wt% in β-stishovite at the base of the lower mantle (130 GPa) (Fig. 5a). Based on current rates of crustal production and subduction, we estimate the maximum mass of H_2O that can enter the lower mantle stored in stishovite to be of the order 3.5 $\times 10^{11}$ kg/yr (Fig. 5b), which is sufficient to host all of the crustal H_2O that would otherwise be released by 300 km because of lawsonite or phengite dehydration. Stabilization of an Fe-Ti oxyhydroxide in the transition zone may also enhance the storage capacity even further, even though its modal abundance will be only a few percent at most (Liu et al., 2017).

Stishovite alone can also accommodate all of the H_2O released from the mantle portion of the slab at the base of the transition zone and shallow lower mantle if H_2O-rich fluids or hydrous silicate melts migrate into the adjacent oceanic crust, possibly along pre-existing fracture systems related to lithospheric hydration. Once oceanic crust enters the lower mantle, aluminous phase
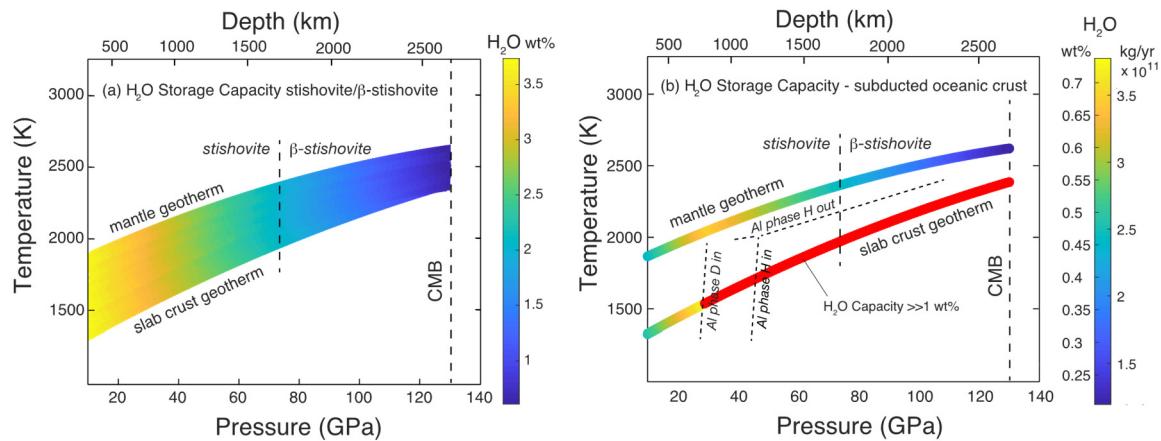
Fig. 5. (a) H_2O storage capacity (wt%) in stishovite and β-stishovite calculated from equation (3) for pressures and temperatures between model geotherms for the convecting mantle (Katsura et al., 2010) and for the top of oceanic crust in a cold slab (Shirey et al., 2021) extrapolated to the core mantle boundary. H_2O contents are given by the color scale. (b) Estimated storage capacity of oceanic crust (basalt/gabbro + sediment). We assume a modal mineralogy of SiO_2 phases in basaltic crust of 10 wt% at 10 GPa increasing linearly to 20 wt% at 30 GPa and remaining constant to 130 GPa based on experimental phase relations (Ono, 1998; Ono et al., 2001; Perrillat et al., 2006). For the sediment we assume SiO_2 constitutes 30 wt% of the mode throughout the upper and lower mantle (Irifune et al., 1994; Ono, 1998). The H_2O content in stishovite/β-stishovite is calculated from equation (3) as shown in (a). We use a conservative estimate for the H_2O storage capacity for the remaining nominally anhydrous phases in oceanic crust (e.g. cpx, majorite, bridgmanite, Ca-perovskite, NAL/CF phases, hollandite, CAS phase) of 1000 ppm for all phases as these are generally poorly constrained, and where measured are in the range of <100 to >2000 ppm (Bolfan-Casanova et al., 2000; Fu et al., 2019; Litasov et al., 2003; Murakami et al., 2002; Panero et al., 2015). The current mass of subducted basaltic oceanic crust is estimated at 5×10^{13} kg/yr (van Keken et al., 2011) and terrigenous pelagic sediment at 1.1×10^{12} kg/yr (Rea and Ruff, 1996). Also shown are boundaries estimating where aluminous phase D (Pamato et al., 2015) and aluminous phase H (Walter et al., 2015) stabilize in basaltic oceanic crust and the melting curve of phase H (Walter et al., 2015). Once these hydrous phases stabilize in oceanic crust the overall H_2O storage capacity increases dramatically as depicted in (b).

D ($\sim$25 GPa) (Pamato et al., 2015) and aluminous phase H (>$\sim$45 GPa) (Nishi et al., 2014; Walter et al., 2015) stabilize and have much higher H_2O storage capacities, $\sim$15 wt% each, endowing the crust with a very large H_2O storage capacity throughout the lower mantle (Ohtani, 2015). We note, however, that these hydrous phases will not stabilize until SiO_2 phases are saturated with H_2O as dictated by chemography (e.g., Walter et al., 2015).

Because aluminous phase H is stable throughout the lower mantle depth range, deeply subducted oceanic crust may retain all its H_2O to the core mantle boundary (Ohira et al., 2014; Ohtani, 2015; Walter et al., 2015). However, if the slab crust thermally equilibrates with the convecting mantle as it transits the lower mantle, phase H may breakdown to form a hydrous melt (Walter et al., 2015), whereas β-stishovite will remain stable even at the high temperatures of the geotherm and retain some of the H_2O, with some released into the lower mantle. Release of hydrous fluids or melt into the surrounding mantle will result in hydration through reaction with iron metal (Zhu et al., 2019) and silicate phases like bridgmanite and Ca-perovskite if these phases are undersaturated, which might be expected if the lower mantle after accretion crystallized relatively dry as a consequence of its high solidus and liquidus temperature (Dong et al., 2021). If the lower mantle phases are already saturated then H_2O would remain in a partial melt because no other hydrous phases are stable at temperatures along the mantle geotherm (Walter et al., 2015).

The high H_2O storage capacity of stishovite in oceanic crust provides a conduit for water transport from the upper mantle to the core mantle boundary. Over 4 Ga of subduction, about 1.4×10^{21} kg of H_2O can be added to the lower mantle transported in stishovite alone at current crustal production rates, or about one ocean mass. One ocean mass is similar to the total amount of H_2O predicted to be added to the deep mantle over $\sim$4 Ga of subduction based on modern H_2O fluxes calculated from phase equilibria and thermal models (Hacker, 2008; Rupke et al., 2004; van Keken et al., 2011) and is remarkably close to the total mantle H_2O content predicted on the basis of H_2O/CeO in mantle derived magmas (Hirschmann, 2018). Subduction of H_2O to the CMB primarily hosted by β-stishovite may also potentially ex-

plain the higher average H_2O content in the source of ocean island basalts if they originate from plumes sourced in the deep lower mantle (Hirschmann, 2006).

Once the subducted slab reaches the core mantle boundary, if the temperature of the crust remains below phase H dehydration, then effectively all the H_2O deposited in the crust in the upper mantle can survive to the core mantle boundary (up to 3.5×10^{11} kg/yr). If phase H is no longer stable, then oceanic crust can transport $\sim$0.2 wt% H_2O ($\sim$1 $\times$ 10^{11}$ kg/yr) primarily in β-stishovite (Fig. 3b). The high temperature of the outer core ($\sim$4000 K) creates a super-adiabatic temperature gradient above the core (Hirose et al., 2013), which will induce phase H and possibly β-stishovite to dehydrate as crust stagnates at the CMB. Reaction of released water with the iron-metal of the core may add hydrogen to the outer core if it is undersaturated or crystallize new high-pressure phases such as FeO_2H_x and FeH_5 (Hu et al., 2016; Liu et al., 2017; Mao et al., 2017; Nishi et al., 2017; Pepin et al., 2017; Mao and Mao, 2020; Hu and Mao, 2021). Production of hydrous partial melt and iron hydride phases have both been shown to provide plausible explanations for the observed seismic anisotropy (Kendall and Silver, 1996) and anomalously slow P-wave velocities (Williams and Garnero, 1996) at the base of Earth's mantle. Thus, these features may be a hallmark of H_2O subducted from the surface to the core-mantle boundary, with hydrous SiO_2 phases the key hosts for transporting H_2O from the upper mantle into the lower mantle.

CRediT authorship contribution statement

Yanhao Lin: Conceptualization, Methodology, Visualization, Writing – original draft, Writing – review & editing. **Qingyang Hu:** Conceptualization, Methodology, Visualization, Writing – original draft, Writing – review & editing. **Michael J. Walter:** Conceptualization, Methodology, Visualization, Writing – original draft, Writing – review & editing. **Jing Yang:** Methodology. **Yue Meng:** Methodology. **Xiaolei Feng:** ab initio simulations. **Yukai Zhuang:** Methodology. **R.E. Cohen:** ab initio simulations, review & editing. **Ho-Kwang Mao:** Conceptualization, Methodology, Visualization, Writing – review & editing.

Declaration of competing interest

Acknowledgements

Appendix A. Supplementary material

Supplementary material related to this article can be found online at https://doi.org/10.1016/j.epsl.2022.117708.

References

Alt, J.C., Schwarzenbach, E.M., Frueh-Green, G.L., Shanks, W.C., Bernasconi, S.M., Garrido, C.J., Crispini, L., Gaggero, L., Padron-Navarta, J.A., Marchesi, C., 2013. The role of serpentinites in cycling of carbon and sulfur: seafloor serpentinization and subduction metamorphism. Lithos 178, 40–54.

Alt, J.C., Teagle, D.A.H., 2003. Hydrothermal alteration of upper oceanic crust formed at a fast-spreading ridge: mineral, chemical, and isotopic evidence from ODP Site 801. Chem. Geol. 201, 191–211.

Andrault, D., Angel, R.J., Mosenfelder, J.L., Le Bihan, T., 2003. Equation of state of stishovite to lower mantle pressures. Am. Mineral. 88, 301–307.

Bina, C.R., 1997. Patterns of deep seismicity reflect buoyancy stresses due to phase transitions. Geophys. Res. Lett. 24, 3301–3304.

Bolfan-Casanova, N., Keppler, H., Rubie, D.C., 2000. Water partitioning between nominally anhydrous minerals in the MgO-SiO2-H2O system up to 24 GPa: implications for the distribution of water in the Earth's mantle. Earth Planet. Sci. Lett. 182, 209–221.

Bromiley, G.D., Bromiley, F.A., Bromiley, D.W., 2006. On the mechanisms for H and Al incorporation in stishovite. Phys. Chem. Miner. 33, 613–621.

Caracas, R., Panero, W.R., 2017. Hydrogen mobility in transition zone silicates. Prog. Earth Planet. Sci. 4 (9).

Chung, J.I., Kagi, H., 2002. High concentration of water in stishovite in the MORB system. Geophys. Res. Lett. 29 (21).

Clark, S.J., Segall, M.D., Pickard, C.J., Hasnip, P.J., Probert, M.J., Refson, K., Payne, M.C., 2005. First principles methods using CASTEP. Z. Kristallogr. 220, 567–570.

Dong, J., Fischer, R.A., Stixrude, L.P., Lithgow-Bertelloni, C.R., 2021. Constraining the volume of Earth's early oceans with a temperature-dependent mantle water storage capacity model. AGU Adv. 2, e2020AV000323.

Faccenda, M., 2014. Water in the slab: a trilogy. Tectonophysics 614, 1–30.

Fei, Y., Ricolleau, A., Frank, M., Mibe, K., Shen, G., Prakapenka, V., 2007. Toward an internally consistent pressure scale. Proc. Natl. Acad. Sci. USA 104, 9182–9186.

Fischer, R.A., Campbell, A.J., Chidester, B.A., Reaman, D.M., Thompson, E.C., Pigott, J.S., Prakapenka, V.B., Smith, J.S., 2018. Equations of state and phase boundary for stishovite and CaCl2-type SiO2. Am. Mineral. 103, 792–802.

Fu, S., Yang, J., Karato, S., Vasiliev, A., Presniakov, M.Y., Gavriliuk, A.G., Ivanova, A.G., Hauri, E.H., Okuchi, T., Purevjav, N., Lin, J.F., 2019. Water concentration in single-crystal (Al, Fe)-bearing bridgmanite grown from the hydrous melt: implications for dehydration melting at the topmost lower mantle. Geophys. Res. Lett. 46, 10346–10357.

Gale, A., Dalton, C.A., Langmuir, C.H., Su, Y.J., Schilling, J.G., 2013. The mean composition of ocean ridge basalts. Geochem. Geophys. Geosyst. 14, 489–518.

Grocholski, B., Shim, S.H., Prakapenka, V.B., 2013. Stability, metastability, and elastic properties of a dense silica polymorph, seifertite. J. Geophys. Res., Solid Earth 118, 4745–4757.

Hacker, B.R., 2008. H2O subduction beyond arcs. Geochem. Geophys. Geosyst. 9.

Hirao, N., Kawaguchi, S.I., Hirose, K., Shimizu, K., Ohtani, E., Ohishi, Y., 2020. New developments in high-pressure X-ray diffraction beamline for diamond anvil cell at SPring-8. Matter Radiat. Extrem. 5, 018403.

Hirose, K., Labrosse, S., Hernlund, J., 2013. Composition and state of the core. In: Jeanloz, R. (Ed.), Annual Review of Earth and Planetary Sciences. In: Annual Review of Earth and Planetary Sciences, vol. 41, pp. 657–691.

Hirschmann, M.M., 2006. Water, melting, and the deep Earth H2O cycle. Annu. Rev. Earth Planet. Sci. 34, 629–653.

Hirschmann, M.M., 2018. Comparative deep Earth volatile cycles: the case for C recycling from exosphere/mantle fractionation of major (H2O, C, N) volatiles and from H2O/Ce, CO2/Ba, and CO2/Nb exosphere ratios. Earth Planet. Sci. Lett. 502, 262–273.

Hu, Q., Mao, H.K., 2021. Role of hydrogen and proton transportation in Earth's deep mantle. Matter Radiat. Extrem. 6, 068101.

Hu, Q., Kim, D.Y., Yang, W., Yang, L., Meng, Y., Zhang, L., Mao, H.K., 2016. FeO2 and FeOOH under deep lower-mantle conditions and Earth's oxygen-hydrogen cycles. Nature 534, 241–244.

Irifune, T., Ringwood, A.E., Hibberson, W.O., 1994. Subduction of continental-crust and terrigenous and pelagic sediments - an experimental-study. Earth Planet. Sci. Lett. 126, 351–368.

Iwamori, H., 2004. Phase relations of peridotites under H2O-saturated conditions and ability of subducting plates for transportation of H2O. Earth Planet. Sci. Lett. 227, 57–71.

Katsura, T., Yoneda, A., Yamazaki, D., Yoshino, T., Ito, E., 2010. Adiabatic temperature profile in the mantle. Phys. Earth Planet. Inter. 183, 212–218.

Kendall, J.M., Silver, P.G., 1996. Constraints from seismic anisotropy on the nature of the lowermost mantle. Nature 381, 409–412.

Kingma, K.J., Cohen, R.E., Hemley, R.J., Mao, H.K., 1995. Transformation of stishovite to a denser phase at lower-mantle pressures. Nature 374, 243–245.

Komabayashi, T., Omori, S., 2006. Internally consistent thermodynamic data set for dense hydrous magnesium silicates up to 35 GPa, 1600 degrees C: implications for water circulation in the Earth's deep mantle. Phys. Earth Planet. Inter. 156, 89–107.

Lin, Y., Hu, Q., Meng, Y., Walter, M., Mao, H.K., 2020. Evidence for the stability of ultrahydrous stishovite in Earth's lower mantle. Proc. Natl. Acad. Sci. USA 117, 184–189.

Litasov, K., Ohtani, E., Langenhorst, F., Yurimoto, H., Kubo, T., Kondo, T., 2003. Water solubility in Mg-perovskites, and water storage capacity in the lower mantle. Earth Planet. Sci. Lett. 211, 189–203.

Litasov, K.D., Kagi, H., Shatskly, A., Ohtani, E., Lakshtanov, D.L., Bass, J.D., Ito, E., 2007. High hydrogen solubility in A1-rich stishovite and water transport in the lower mantle. Earth Planet. Sci. Lett. 262, 620–634.

Liu, J., Hu, Q., Kim, D.Y., Wu, Z., Wang, W., Xiao, Y., Chow, P., Meng, Y., Prakapenka, V.B., Mao, H.K., Mao, W.L., 2017. Hydrogen-bearing iron peroxide and the origin of ultralow-velocity zones. Nature 551, 494–497.

Mao, H.K., Hu, Q., Yang, L., Liu, J., Kim, D.Y., Meng, Y., Zhang, L., Prakapenka, V.B., Yang, W.G., Mao, W.L., 2017. When water meets iron at Earth's core-mantle boundary. Nat. Sci. Rev. 4, 870–878.

Mao, H.K., Mao, W.L., 2020. Key problems of the four-dimensional Earth system. Matter Radiat. Extrem. 5, 038102.

Meng, Y., Shen, G., Mao, H.K., 2006. Double-sided laser heating system at HPCAT for in situ x-ray diffraction at high pressures and high temperatures. J. Phys. Condens. Matter 18, S1097–S1103.

Murakami, M., Hirose, K., Ono, S., Ohishi, Y., 2003. Stability of CaCl2-type and alpha-PbO2-type SiO2 at high pressure and temperature determined by in-situ X-ray measurements. Geophys. Res. Lett. 30, 1207.

Murakami, M., Hirose, K., Yurimoto, H., Nakashima, S., Takafuji, N., 2002. Water in Earth's lower mantle. Science 295, 1885–1887.

Nishi, M., Irifune, T., Tsuchiya, J., Tange, Y., Nishihara, Y., Fujino, K., Higo, Y., 2014. Stability of hydrous silicate at high pressures and water transport to the deep lower mantle. Nat. Geosci. 7, 224–227.

Nishi, M., Kuwayama, Y., Tsuchiya, J., Tsuchiya, T., 2017. The pyrite-type high-pressure form of FeOOH. Nature 547, 205–208.

Nishihara, Y., Matsukage, K.N., 2016. Iron-titanium oxyhydroxides as water carriers in the Earth's deep mantle. Am. Mineral. 101, 919–927.

Nisr, C., Chen, H.W., Leinenweber, K., Chizmeshya, A., Prakapenka, V.B., Prescher, C., Tkachev, S.N., Meng, Y., Liu, Z.X., Shim, S.H., 2020. Large H2O solubility in dense silica and its implications for the interiors of water-rich planets. Proc. Natl. Acad. Sci. USA 117, 9747–9754.

Nisr, C., Leinenweber, K., Prakapenka, V., Prescher, C., Tkachev, S., Shim, S.H.D., 2017a. Phase transition and equation of state of dense hydrous silica up to 63 GPa. J. Geophys. Res., Solid Earth 122, 6972–6983.

Nisr, C., Shim, S.H., Leinenweber, K., Chizmeshya, A., 2017b. Raman spectroscopy of water-rich stishovite and dense high-pressure silica up to 55 GPa. Am. Mineral. 102, 2180–2189.

Nomura, R., Hirose, K., Sata, N., Ohishi, Y., 2010. Precise determination of post-stishovite phase transition boundary and implications for seismic heterogeneities in the mid-lower mantle. Phys. Earth Planet. Inter. 183, 104–109.

Ohira, I., Ohtani, E., Sakai, T., Miyahara, M., Hirao, N., Ohishi, Y., Nishijima, M., 2014. Stability of a hydrous delta-phase, AlOOH-MgSiO$_2$(OH)$_2$, and a mechanism for water transport into the base of lower mantle. Earth Planet. Sci. Lett. 401, 12–17.

Ohtani, E., 2015. Hydrous minerals and the storage of water in the deep mantle. Chem. Geol. 418, 6–15.

Okamoto, K., Maruyama, S., 1999. The high-pressure synthesis of lawsonite in the MORB+H$_2$O system. Am. Mineral. 84, 362–373.

Okamoto, K., Maruyama, S., 2004. The eclogite-gametite transformation in the MORB+H$_2$O system. Phys. Earth Planet. Inter. 146, 283–296.

Omori, S., Komabayashi, T., Maruyama, S., 2004. Dehydration and earthquakes in the subducting slab: empirical link in intermediate and deep seismic zones. Phys. Earth Planet. Inter. 146, 297–311.

Ono, S., 1998. Stability limits of hydrous minerals in sediment and mid-ocean ridge basalt compositions: implications for water transport in subduction zones. J. Geophys. Res., Solid Earth 103, 18253–18267.

Ono, S., Ito, E., Katsura, T., 2001. Mineralogy of subducted basaltic crust (MORB) from 25 to 37 GPa, and chemical heterogeneity of the lower mantle. Earth Planet. Sci. Lett. 190, 57–63.

Pamato, M.G., Myhill, R., Ballaran, T.B., Frost, D.J., Heidelbach, F., Miyajima, N., 2015. Lower-mantle water reservoir implied by the extreme stability of a hydrous aluminosilicate. Nat. Geosci. 8, 75–79.

Panero, W.R., Benedetti, L.R., Jeanloz, R., 2003. Transport of water into the lower mantle: role of stishovite. J. Geophys. Res., Solid Earth 108, 2039.

Panero, W.R., Pigott, J.S., Reaman, D.M., Kabbes, J.E., Liu, Z., 2015. Dry (Mg, Fe)SiO$_3$ perovskite in the Earth's lower mantle. J. Geophys. Res., Solid Earth 120, 894–908.

Pawley, A.R., McMillan, P.F., Holloway, J.R., 1993. Hydrogen in stishovite, with implications for mantle water content. Science 261, 1024–1026.

Pepin, C.M., Geneste, G., Dewaele, A., Mezouar, M., Loubeyre, P., 2017. Synthesis of FeH$_5$: a layered structure with atomic hydrogen slabs. Science 357, 382–385.

Perrillat, J.P., Ricolleau, A., Daniel, I., Fiquet, G., Mezouar, M., Guignot, N., Cardon, H., 2006. Phase transformations of subducted basaltic crust in the upmost lower mantle. Phys. Earth Planet. Inter. 157, 139–149.

Poli, S., Schmidt, M.W., 2002. Petrology of subducted slabs. Annu. Rev. Earth Planet. Sci. 30, 207–235.

Prescher, C., Prakapenka, V.B., 2015. DIOPTAS: a program for reduction of two-dimensional X-ray diffraction data and data exploration. High Press. Res. 35, 223–230.

Rea, D.K., Ruff, L.J., 1996. Composition and mass flux of sediment entering the world's subduction zones: implications for global sediment budgets, great earthquakes, and volcanism. Earth Planet. Sci. Lett. 140, 1–12.

Rupke, L.H., Morgan, J.P., Hort, M., Connolly, J.A.D., 2004. Serpentine and the subduction zone water cycle. Earth Planet. Sci. Lett. 223, 17–34.

Schmidt, M.W., Poli, S., 2003. Generation of mobile components during subduction of oceanic crust. In: Rudnick, R. (Ed.), Treatise on Geochemistry, vol. 3, The Crust. Elsevier, New York.

Shirey, S.B., Wagner, L.S., Walter, M.J., Pearson, D.G., van Keken, P.E., 2021. Slab transport of fluids to deep focus earthquake depths – thermal modeling constraints and evidence from diamonds. AGU Adv. 2, e2020AV000304.

Spektor, K., Nylen, J., Mathew, R., Eden, M., Stoyanov, E., Navrotsky, A., Leinenweber, K., Haussermann, U., 2016. Formation of hydrous stishovite from coesite in high-pressure hydrothermal environments. Am. Mineral. 101, 2514–2524.

Spektor, K., Nylen, J., Stoyanov, E., Navrotsky, A., Hervig, R.L., Leinenweber, K., Holland, G.P., Haussermann, U., 2011. Ultrahydrous stishovite from high-pressure hydrothermal treatment of SiO$_2$. Proc. Natl. Acad. Sci. USA 108, 20918–20922.

Sun, N., Shi, W., Mao, Z., Zhou, C., Prakapenka, V.B., 2019. High pressure-temperature study on the thermal equations of state of seifertite and CaCl$_2$-type SiO$_2$. J. Geophys. Res., Solid Earth 124, 12620–12630.

van Keken, P.E., Hacker, B.R., Syracuse, E.M., Abers, G.A., 2011. Subduction factory: 4. Depth-dependent flux of H$_2$O from subducting slabs worldwide. J. Geophys. Res., Solid Earth 116, B01401.

Wada, I., Behn, M.D., Shaw, A.M., 2012. Effects of heterogeneous hydration in the incoming plate, slab rehydration, and mantle wedge hydration on slab-derived H$_2$O flux in subduction zones. Earth Planet. Sci. Lett. 353, 60–71.

Walter, M.J., 2021. Water transport to the core-mantle boundary. Nat. Sci. Rev. 8, nwab007.

Walter, M.J., Thomson, A.R., Wang, W., Lord, O.T., Ross, J., McMahon, S.C., Baron, M.A., Melekhova, E., Kleppe, A.K., Kohn, S.C., 2015. The stability of hydrous silicates in Earth's lower mantle: experimental constraints from the systems MgO-SiO$_2$-H$_2$O and MgO-Al$_2$O$_3$-SiO$_2$-H$_2$O. Chem. Geol. 418, 16–29.

Williams, Q., Garnero, E.J., 1996. Seismic evidence for partial melt at the base of Earth's mantle. Science 273, 1528–1530.

Wolanin, E., Pruzan, P., Chervin, J.C., Canny, B., Gauthier, M., Hausermann, D., Hanfland, M., 1997. Equation of state of ice VII up to 106 GPa. Phys. Rev. B 56, 5781–5785.

Yoshino, T., Manthilake, G., Matsuzaki, T., Katsura, T., 2008. Dry mantle transition zone inferred from the conductivity of wadsleyite and ringwoodite. Nature 451, 326–329.

Zhu, F., Li, J., Liu, J., Dong, J., Liu, Z., 2019. Metallic iron limits silicate hydration in Earth's transition zone. Proc. Natl. Acad. Sci. USA 116, 22526–22530.